2D Materials

PAPER

RECEIVED
28 August 2023

REVISED
18 October 2023

ACCEPTED FOR PUBLICATION
23 November 2023

PUBLISHED
5 December 2023

Higher-order obstructed atomic insulator phase in pentagonal monolayer $PdSe_2$

Victor Nuñez[1], Sergio Bravo[1,*], J D Correa[2], Leonor Chico[3,*] and M Pacheco[1,*]

[1] Departamento de Física, Universidad Técnica Federico Santa María, Casilla 110 V, Valparaíso, Chile
[2] Facultad de Ciencias Básicas, Universidad de Medellín, Medellín, Colombia
[3] IGISC, Departamento de Física de Materiales, Facultad de Ciencias Físicas, Universidad Complutense de Madrid, 28040 Madrid, Spain
[*] Authors to whom any correspondence should be addressed.

E-mail: monica.pacheco@usm.cl, leochico@ucm.es and sergio.bravoc@usm.cl

Keywords: SSH model, higher order topology, pentagonal materials

Supplementary material for this article is available online

Abstract

We investigate a pentagonal monolayer of palladium diselenide, a stable two-dimensional system, as a material realization of a crystalline phase with nontrivial topological electronic properties. We find that its electronic structure involves an atomic obstructed insulator related to higher-order topology, which is a consequence of the selenium-selenium bond dimerization along with inversion and time-reversal symmetry). By means of first-principles calculations and the analysis of symmetry indicators and topological invariants, we also characterize the electronic corner states associated with the atomic obstruction and compute the corresponding corner charge for a finite geometry, which is found to be not quantized but still inversion-protected. Applying tensile strain to the finite geometry we verify the robustness of the corner states and also achieve a strain-controlled variation of the corner charge magnitude.

1. Introduction

In recent years the realization of topological phases of matter in crystalline structures has unleashed a paradigm shift in materials research due to the promising technological and scientific applications that these systems could furnish. Several types of topologically nontrivial systems have been discovered over the past decades, such as Chern insulators, spin Hall insulators, topological semimetals, topological superconductors and topological crystalline insulators, just to name a few instances. In particular, topological crystalline insulators have been identified as a family of systems for which crystalline symmetry is a crucial ingredient, since it allows for topologically protected states [1]. Within this broad group of materials, there exists a subgroup of crystalline insulators that can exhibit what is called higher-order topology (HOT) [2]. This higher-order attribute implies that the nontrivial response is realized when the bulk system is embedded in a $(d-k)$-dimensional geometry, where k labels the order of the topological insulator [3]. In the case of two periodic dimensions in real space, $d=2$, one encounters that systems with HOT have finite systems which present zero-dimensional states with nontrivial properties, such as corner states and corner charges [4]. These HOT structures represent a class known as two-dimensional (2D) obstructed atomic insulators (OAI) [5], which are defined as insulators whose electronic structure can be described by a set of atomic orbitals (Wannier functions), some of them located away from the atomic positions of the material [5, 6]. Several systems with obstructed higher-order phases have been proposed recently. Particular examples are graphdyine [7, 8], graphyne [9], phosphorene [10], Xenes [11], transition metal dichalcogenides [12–14] and also other families of materials, such as those described in [15–18]. Along this line, in what follows, we report on the realization of an OAI phase in pentagonal palladium diselenide ($PdSe_2$) in its monolayer form. This material is appealing since it has been recently synthesized in bulk and layered samples [19, 20]. It is also the first experimental realization of a family of computationally proposed systems known as pentagonal materials, which have a lattice structure resembling the Cairo tiling [21]. In particular, pentagonal $PdSe_2$ has been characterized to have notable electrical and

optical transport characteristics [19], and good thermoelectric properties [22]. Most importantly, it is stable in the air, so it can be explored for applications of topological 2D pentagonal materials. In light of the promising features that $PdSe_2$ entails, a topological characterization, analyzing the possible nontrivial phases that can coexist, will add valuable insights to previous findings and put forward guidelines for novel potential applications. Thus, the HOT phase encountered in this work coexists with another topological phase in the same material, as reported in [23]. This establishes pentagonal $PdSe_2$ as a platform to study diverse topological phenomena and their physical implications.

The organization of the article is as follows. First, we present the real-space properties of the material, including lattice symmetries and the preponderant orbital features of interest. Next, we analyze the properties of the system by means of first-principles electronic structure calculations, including band structure and other electronic properties. Additionally, we perform a topological characterization using the well-established theories of symmetry-indicated band topology, as presented in [5, 24, 25]. Topological invariants suitable for the identification of the nontrivial phases are calculated. Further first-principles calculations in a finite geometry will be presented, comprising eigenvalues and charge analysis, in order to explore the properties of the crystalline higher-order topological phase of the material. Additional details of the main text results are available in the supplementary information.

2. Basic properties of monolayer $PdSe_2$

We focus on $PdSe_2$ monolayer, a 2D material with a pentagonal lattice structure composed of palladium and selenium atoms. The lattice structure is formed by irregular type-2 pentagons with buckled geometry, as presented in figure 1(a). Palladium atoms have coordination number 4, while Se atoms possess coordination number 3. Crystalline 2D pentagonal $PdSe_2$ has a tetragonal lattice with three symmetry operations [20] besides identity: spatial inversion I and two non-symmorphic operations, namely, a π rotation about an axis along the $\boldsymbol{a}_1$ direction followed by a half translation, $(C_2|1/2, 1/2)$, and a mirror reflection of a plane perpendicular to the $\boldsymbol{a}_1$ direction combined with a half translation, $(M_y|1/2, 1/2)$. The fractional translation vector in these two last operations is expressed in terms of the unit cell vectors, $\boldsymbol{a}_1$ and $\boldsymbol{a}_2$, respectively. These symmetries compose the space group (SG) $P2_1/c$, also denoted as SG 14. The four chalcogen atoms in the unit cell are interchanged by the symmetries of the SG and should be collectively identified by the generic Wyckoff position (WP) 4e, following the notation of [26]. The transition metal atoms sit at a maximal WP, the 2c position in our unit cell choice. The location of the WP of interest for this work is sketched in figure 1(b).

From a chemical perspective the buckled pentagonal tiling shows two main types of direct bonds, Se–Se and Se–Pd bonds, as seen in figure 1(a). We have verified that low-energy physics is mainly described by the Se–Se dimers which are the strongest bonds. This implies that the Se p-orbitals play the most significant role for the top valence bands and low-lying conduction bands, as detailed in the results below. To corroborate the dimerized nature of $PdSe_2$ monolayer we analyze the difference between the Se–Se and Se–Pd bonds by means of first-principles calculations.

Being a pentagonal $PdSe_2$ monolayer a 2D material, a signature of its HOT would be the appearance of zero-dimensional localized states, i.e. corner charges. Indeed, the dimensional hierarchy in topological 2D materials implies that a first-order topological 2D system will hold edge states, whereas a second-order topological character manifests in the occurrence of corner states, as schematically depicted in figure 1(c).

3. Results

In general, obstructed phases can be linked to the presence of anomalous localization of the electronic charge centers concerning the atomic sites. This charge center mismatch is the basic signature of an atomic obstructed insulator [5].

The identification of a potential obstructed phase requires in the first place to carry out an electronic characterization of the material. From the electronic structure calculations, the symmetry of the states in real and momentum space can be obtained. This symmetry information indicates whether this anomalous charge localization is unavoidable or not.

Second, we have to compute a topological invariant derived from the bulk information of the material (the monolayer in this case) and find out whether it has a nontrivial value. This allows us to identify the specific phase realized by $PdSe_2$. If the invariant indicates a nontrivial behavior, physical manifestations of this characteristic must be identified. In fact, in 2D OAI systems nontrivial states have a higher-order character. That is to say, there must exist a symmetry-protected feature in zero-dimensional systems derived from these OAIs, also known as flakes or quantum dots, which are finite in all spatial dimensions. The existence of corner states is a physical consequence of an OAI. In what follows, we detail this procedure for $PdSe_2$.

3.1. Electronic characterization

We start by presenting in figure 2(a) the characterization of the bonding information in $PdSe_2$ arising from the electron localization function [27]. It can be

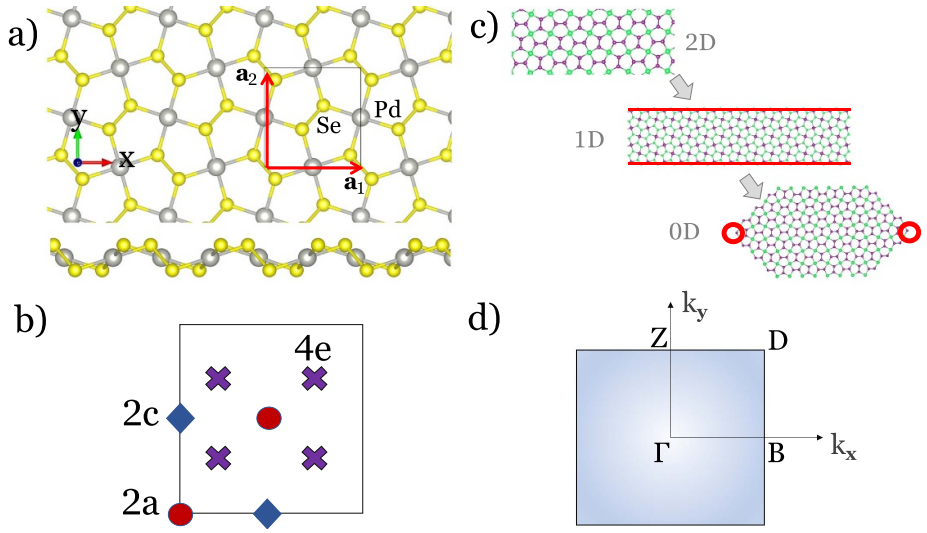

Figure 1. (a) The lattice structure of monolayer $PdSe_2$. (b) Wyckoff positions for the two-dimensional version of space group 14. (c) Schematic depiction of the dimensional hierarchy in topological 2D materials, particularized for $PdSe_2$. (d) Two-dimensional Brillouin zone.

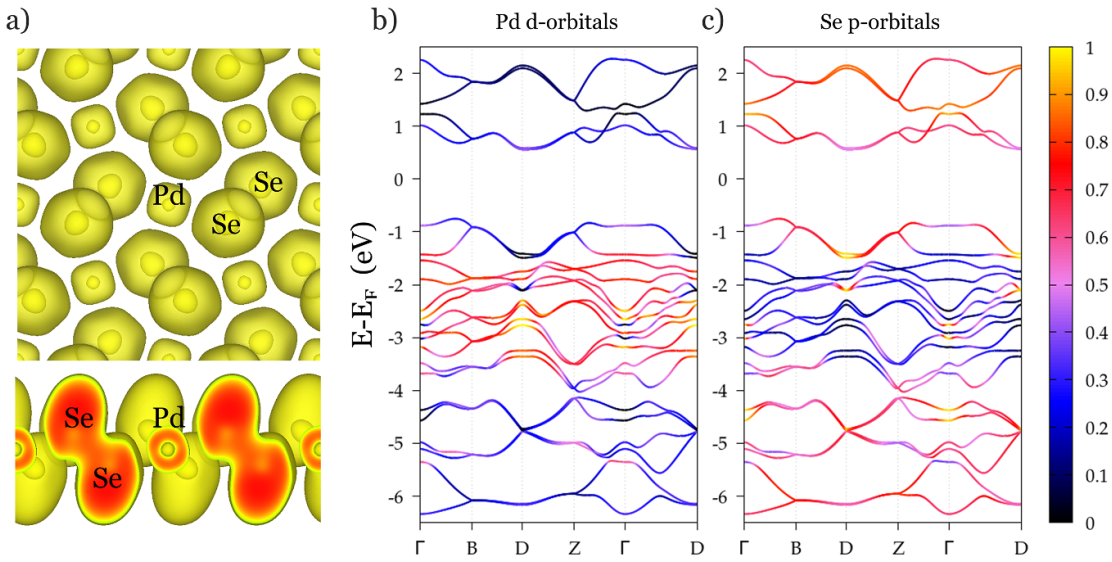

Figure 2. (a) Electron localization function. Electronic bands from first principles including SOC with k-resolved projected density of states (k-PDOS) for (b) Pd *d*-orbitals and (c) Se *p*-orbitals.

observed that the tendency of the electrons to localize outside the atomic sites occurs mostly along the direct Se–Se bonds, while the regions corresponding to Pd–Se bonds are mostly depleted. This indicates the special role played by the Se–Se interaction in the physics of $PdSe_2$. In fact, these Se-Se dimers effectively realize a material example of a 2D version of the Su–Schrieffer–Heeger (SSH) model, similar to the cases reported in [28–32]. The resemblance with the SSH model stands as a starting guide to explore nontrivial electronic states, since SSH systems can present obstructed phases [29, 31].

To confirm the presence of the aforementioned phase we study the electronic band structure of the material obtained from density functional theory calculations along a high-symmetry path in the Brillouin zone, as specified in figure 1(d). The band structures computed including spin-orbit (SOC) coupling are shown in figure 2. The bands without SOC is presented in the supplementary information. Our calculation confirms an indirect fundamental gap of approximately 1.3 eV employing a Perdew–Burke–Ernzerhof (PBE) functional [33], as previously noted in other studies [19]. While higher gaps have been reported using hybrid functionals or many-body correlations, we stay with the PBE results since the valence bands are well-described at this level of approximation.

Table 1. Band representations (BR) present in the valence band manifold of monolayer $PdSe_2$. The first column gives the irreps content for each BR, the second column shows the number of occurrences for a particular BR, and the third column links the BR with the respective inducing Wyckoff position. The last two BRs cannot be induced from EBRs, and thus are stable topological ($Z_2 = 1$). However, as they are both below the Fermi level they add to a trivial phase, which can in principle be induced from one EBR from 2a WP plus another EBR from 2c WP.

Band representations	Multiplicity	Inducing WP
$2\Gamma_3\Gamma_4$—$D_3D_3D_4D_4$	3	2a
$2\Gamma_3\Gamma_4$—$D_5D_5D_6D_6$	5	2c
$2\Gamma_5\Gamma_6$—$D_3D_3D_4D_4$	4	2c
$2\Gamma_5\Gamma_6$—$D_5D_5D_6D_6$	1	2a
$\Gamma_3\Gamma_4\Gamma_5\Gamma_6$—$D_5D_5D_6D_6$	1	—
$\Gamma_3\Gamma_4\Gamma_5\Gamma_6$—$D_5D_5D_6D_6$	1	—

Bearing in mind that the material belongs to SG 14, we can deduce certain characteristics of its electronic properties. To start, we observe that the nonsymmorphic symmetries fix the multiplicity of the maximal WP to two. This can be combined with the spinful (spinless) features of the material and with time-reversal symmetry (TRS). With all this information we can conclude that, for the generic 4e WP, the orbitals must form groups of eight (four). On the other hand, orbitals must form groups of four (two). From the symmetry-based topological band theory [5, 34] it is known that the maximal WP induce the so-called elementary band representations (EBRs), from which some generic bands can be formed and analyzed. Combining the orbital input with the band details immediately leads us to the conclusion that all bands must appear as four-connected sets. The actual symmetry data can be extracted from the electronic structure calculations in momentum space. In particular, we have computed the symmetry eigenvalues and corresponding irreducible representations (irreps) for the high-symmetry points (HSP) of the material. The results are presented in table 1 for the valence bands of interest. In this table, we present the multiplicity of each EBR within the valence band manifold of monolayer $PdSe_2$. It is worth noticing that all connected sets of bands are EBRs. This implies that the valence band manifold realizes an atomic limit. However, it is readily seen that some of the EBRs must be induced by orbitals located at the unoccupied WP 2a. What is more, this 2a WP lies at the middle point of the line that forms the Se–Se bond. In consequence, information extracted from the electronic structure suggests that there is an unavoidable contribution of unoccupied sites in real space.

3.2. Identification of OAIs: topological invariants

The procedure for a system with and without SOC is similar, since the definition of the invariant only involves counting eigenvalues. The difference stems from the labels of irreps. Using that inversion symmetry is part of the SG, we could use inversion-based symmetry invariants to prove the obstruction. For this, we follow [3, 35], and start from the standard Wilson loop (WL) invariants, that are suitable for the study of this model. A simplified version of these WL invariants will be used due to the existence of inversion symmetry. First, we have to consider that the WL should be defined for particular directions in reciprocal space. There are two directions in our case, k_x and k_y; see figure 1(c). The k_x direction is related with Γ and B HSP, while k_y is related with Γ and Z points. Then, each direction yields one topological invariant, respectively denoted as ν_B and ν_Z [35]. A third invariant is related to the nested WL [3]. This last invariant gives information about the multipole properties of the system [35], and is related to the Γ and D HSP. It is denoted as ν_D. Thus, overall, we have at our disposal three topological indices. For inversion symmetric systems, the general form of the invariants is $\nu_\Lambda = \#\Lambda - \#\Gamma$ (valid with and without SOC), where $\#A$ is the number of inversion-odd eigenvalues at point A in momentum space [36]. The information about these eigenvalues can be extracted from the irreps calculation that was presented before.

The computation of the above WL invariants for $PdSe_2$ yields $\nu_B = 1$ and $\nu_Z = 1$, confirming the nontrivial character of the material. The remaining invariant is calculated to be $\nu_D = 0$. This last invariant is related to the presence of a bulk quadrupole moment [36]. In summary, the SG 14 obstructed phases can be characterized by three invariants, (ν_B, ν_Z, ν_D), and monolayer $PdSe_2$ realizes the nontrivial phase $(1, 1, 0)$. This phase implies formally the presence of edges polarizations and no quadrupole moment.

A complementary perspective can be gained by invoking the aforementioned relation to the SSH model. The nontrivial SSH phase host states that have formal polarizations with values of 0 or 1/2 (modulo 1) [29], a fact that is related to the 0 and π restriction of the Zak phase in momentum space. Therefore, it is the π Zak phase of the SSH model which is related to nontrivial behavior. In addition, WL is directly linked to the Zak phase of quasi-one-dimensional systems that are localized in one direction and delocalized along the other. This is because WL is constructed from hybrid Wannier charge centers [37]. Therefore, a nonzero WL invariant value is analogous to having a π obstructed Zak phase.

It is pertinent to introduce a slight simplification at this stage. A correlation, coming from the nonsymmorphic bulk SG, arises between the number of odd-inversion eigenvalues at B and Z; they are always equal. This is due to the fact that the type of irreducible representations at both points always

coincide, both for the spinless and spinful cases. In consequence, the system at hand satisfies the condition $\nu_B = \nu_Z$, and the classification is simplified to only two indices (ν_B, ν_D). Considering this, the $PdSe_2$ phase can be labeled as $(1,0)$.

3.3. Characterization of OAIs: corner response

In general bulk-boundary correspondence implies the existence of a low-dimensional anomalous boundary state (1D or 0D) in a system with a nontrivial bulk (in this case 2D). The anomalous states could be edge states or corner states, according to the case. The correspondence is characterized by a number that indicates a property of the boundary system, based on features deduced from the bulk structure. For example, in Chern insulators, the indicator is the Chern number, and its magnitude indicates the number of gapless states that the system has. In the case of OAIs, which can be related to a higher-order phase, the correspondence is related to the corner charge. Consequently, a bulk number is calculated based on the polarization and quadrupole moment of the system. The physically meaningful (gauge-invariant) combination of these two quantities is defined as the corner charge. Thus, a nontrivial system will manifest a boundary (corner) response due to the nontrivial bulk polarization and/or quadrupole moment.

Therefore, the physical implications of this phase can be related to boundary responses that materialize the obstruction. If we reduce to one dimension, we can construct ribbons with edges having a nonzero polarization. In fact, $PdSe_2$ nanoribbons have been recently synthesized and characterized [38]. However, it has been argued that polarization would not be directly measurable, due to other edge effects and gauge dependence [39]. This also applies in general for the bulk quadrupole moment. On the other hand, fully measurable responses can be linked to the corner states and associated charges that appear at open boundary systems. This is what is called a higher-order bulk-boundary relation [40]. The presence or absence of corner charges is also a topological indicator, since it is related to previous invariants.

A subtle point must be made here in relation to the use of finite systems. Since the SG of the monolayer is nonsymmorphic, as we construct a flake structure, we will invariably break the symmetries that involve fractional translations. Then, in our case, the resulting flakes will have inversion as the only spatial symmetry operation. Therefore, we must study how the properties of SG 14 map to SG 2, the SG with only spatial inversion (and TRS). To establish a link to SG 2 we make use of a procedure dubbed as representation subduction [41]. In simple terms, this method allows mapping the irreps in an SG to the irreps of a subgroup of it. The result of the subduction procedure is as follows:

$$
\begin{aligned}
&\textbf{\textit{SG}14} && \rightarrow \textbf{\textit{SG}2}\\
&\Gamma_3\Gamma_4 && \rightarrow \Gamma_3\Gamma_3\\
&\Gamma_5\Gamma_6 && \rightarrow \Gamma_2\Gamma_2\\
&D_3D_3 && \rightarrow T_3T_3\\
&D_4D_4 && \rightarrow T_3T_3\\
&D_5D_5 && \rightarrow T_2T_2\\
&D_5D_5 && \rightarrow T_2T_2\\
&Z_2Z_2 && \rightarrow Y_2Y_2 + Y_3Y_3\\
&B_2B_2 && \rightarrow Z_2Z_2 + Z_3Z_3.
\end{aligned}
$$

Here the labels T, Y and Z in SG 2 correspond to the same location in the BZ as the original SG 14 points to which they are related by induction.

From this mapping, we can conclude that the distinction between BRs induced from 2a and 2c WP is preserved. This is a significant result that indicates that the phase distinctions arising from bulk topological obstruction can be carried down to low-dimensional systems. For a system with inversion using the simplification in the WL explained before, the corner charge can be defined as

$$Q_c = \frac{\nu_B}{2}\frac{\nu_D}{4}1 \tag{1}$$

for the spinless case [3] and as

$$Q_c^{soc} = \nu_B - \frac{\nu_D}{2}2 \tag{2}$$

for a spinful system [35]. For the $PdSe_2$ monolayer, we obtain $Q_c = 1/2$, $Q_c^{soc} = 1$. A nonzero value of the corner charge invariant implies the presence of protected charges at inversion-related corners of a finite structure. In order to prove this result we have calculated the eigenvalue spectrum for flakes based on the $PdSe_2$ monolayer. We chose a 100-atom flake with two obstructed corners. In practice, the obstructions are implemented by cutting along the dimerized bonds right at the boundary. The resulting eigenvalue spectrum is displayed in figure 3.

It can be observed that the system presents a metallic phase with four degenerate states at the Fermi level. This phenomenon is due to the appearance of a filling anomaly [36]. The metallic states are enforced since the topological obstruction prevents the system to be simultaneously charge-neutral, symmetric, and gapped [42]. Thus one of the features should be put down for the system to be realizable. For this particular flake, the states are localized at the corners, as can be verified in figure 4 where the local density of states of the in-gap states has been plotted.

Another way to extract the quantized value of the corner charge for each state is by means of an eigenvalue calculation. This is related to the Fermi level position of the filling anomaly [42]. Namely, by electron counting, the filling of the flake states means that two of the metallic states must be occupied, leaving two empty states. The energy spectrum

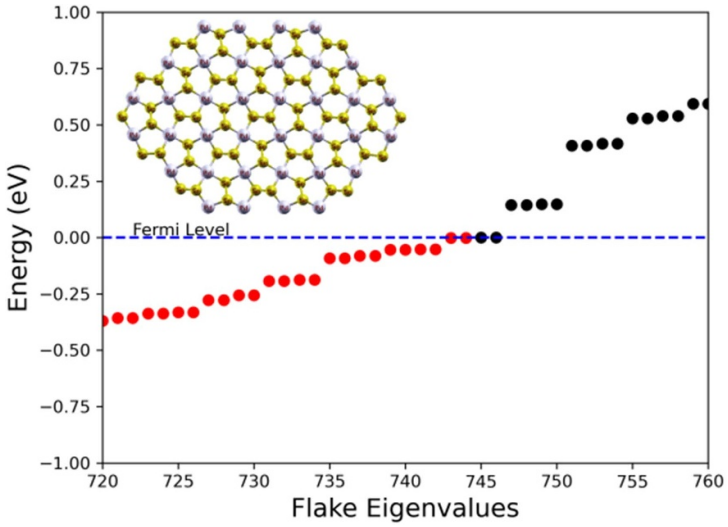

Figure 3. Energy spectrum, where the Fermi level is set at zero energy and marked by a dashed blue line. The inset shows the geometry of the selected 100-atom flake.

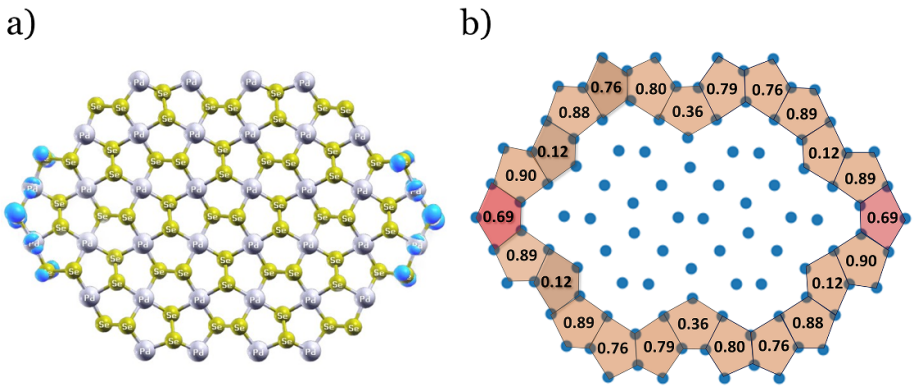

Figure 4. (a) Local density of states (LDOS) close to the Fermi energy for a 100-atom flake. (b) The numerical tile charge calculation for the 100-atom flake. Values within the pentagons represent the charge from Bader analysis modulo 2.

in figure 3 exhibits four degenerate states at the Fermi level. Therefore, two extra electrons must be supplied to resolve the anomaly. This directly indicates that each corner will have a corner charge of one electron, which coincides with the value obtained using equation (2). It should be noted that, since the only spatial symmetry of the finite system is the inversion, the exact value obtained above is in general not protected and deviations from this value are expected [39]. This last result opens the possibility to have fractional charges of equal size at related corners and to control them by external perturbations that preserve inversion.

3.4. Robustness of the obstructed states

Inversion can impose limitations and prohibitions on interactions that might disturb or hybridize the obstructed states. Consequently, obstructed phases can maintain their robustness and preserve their distinctive characteristics under the action of inversion-preserving perturbations. As supporting evidence, to probe the corner states, the $PdSe_2$ flake presented in the previous section was subjected to varying degrees of stress and strain, both in tension and compression. The results for the variation of the eigenvalue spectrum are displayed in figure 5. It can be seen that the energies of the states above or below the Fermi energy, are affected by the perturbation. Remarkably, as we approach the Fermi level the states become more insensitive to strain and this entails that the metallic states are not altered. Thus, for stress and strain respecting spatial inversion the states at the Fermi level remain intact and localized at the corners.

In addition to strain, we examined the response of the flake to structural perturbations such as atomic vacancies. We present one illustrative example in the supplementary information, figure S.4. Note that these vacancies break inversion symmetry. In summary, the results show that the energy spectrum still possesses metallic states if the vacancies do not affect the atomic sites composing the corners. This reinforces the fact that the corner states are highly

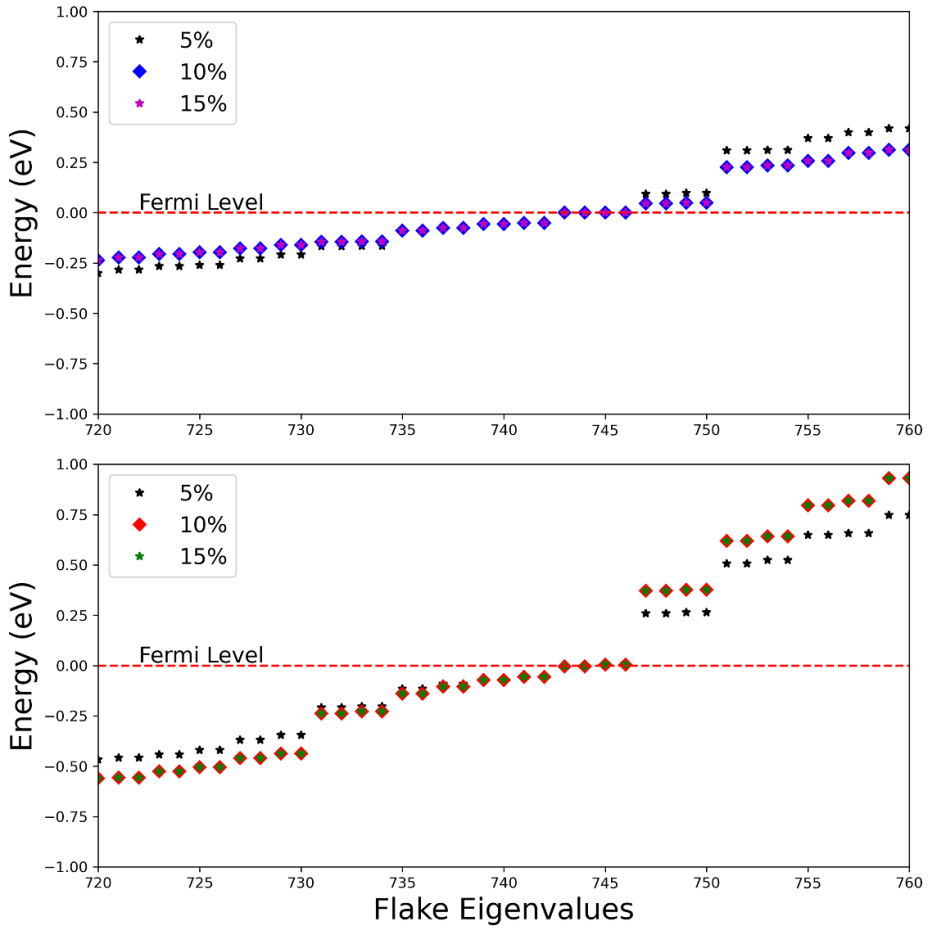

Figure 5. Eigenvalue spectrum of the 100-atom flake of $PdSe_2$ under (a) biaxial tensile stress and (b) biaxial compressive stress.

localized. To test inversion symmetry more dramatically, we have also studied two flakes with a shape that clearly breaks inversion symmetry, by removing one of the regions where the corner states appear (figures S.5 and S.6 of the supplementary information). In these cases the corner states are not present, although the four states at the Fermi energy persist, but their electronic localization changes.

Focusing on the study of corner charge, we have performed a numerical charge analysis for the unstrained and strained flakes with the aim to quantify the corner charge anomaly and the possibility to have a non-quantized value. To this end, we carried standard Voronoi and Bader's calculations to analyze the atomic charge distribution of the flakes. The resulting values of the atomic charges are presented in the supplementary information. Using this charge analysis we compute the numerical value of the corner charge for the flakes by adapting the procedure presented in [43]. In this approach, an effective charge is assigned to the pentagonal units of the flake, considering that the measurable quantity is defined only modulo 2. The results of this process are presented in figure 4(b). It can be seen that these pentagonal tiles form the corners and edges of the flake. The calculation of the corner charge for the flake, Q_c^{flake}, is carried by use of the relation (equation (2) in [43])

$$Q_c^{\text{flake}} = \rho - \left(\sigma_{\text{top}} + \sigma_{\text{bottom}}\right), \tag{3}$$

where ρ is a charge of the corner zone and the σ_i correspond to the net charge of the top and bottom edges, that delimit the corner. As both edges are shared by the left and right corners of the flake, only half of the charge is used in the calculation of Q_c^{flake}. For values of the unstrained flake, we obtain a corner charge of $1.42e$ (mod 2) for both corners, showing the inversion protection of the response. As it was mentioned previously, this value departs from the value deduced from the bulk calculation, since inversion is the only symmetry that survives the dimension reduction. However, we further explore how the non-quantized corner charge is affected by the external strain. We repeat the procedure above for the different values of strain presented in figure 5 and report the corner charges values in table 2. Only the value for one corner is reported, as in all cases inversion-related corners yield the same value. It can be observed that the corner charge can be monotonically varied with positive and negative strain. This behavior along with

Table 2. Numerical corner charge from Bader analysis for different strain applied to the 100-atom flake. Values of the charges are modulo 2.

Strain	0%	−5%	−10%	−15%	+5%
Corner charge	1.45e	1.42e	1.36e	1.27e	1.49e

inversion protection allows for a controllable manipulation of the charge by external means, which gives the possibility of using this mechanism in device applications.

The remarkable localization of the corner states shown in figure 4 is a clear indication of their persistence at larger structures. However, these corner states may hybridize and delocalize if the flake size is reduced. We have performed calculations for smaller sizes and verified that even in 32-atom flakes the corner states remain at the Fermi energy and they are distinguishable, although they start to spread along the edges, see figure S.3 of the supplementary information. Therefore, these states are very robust concerning size reduction. We observe that with respect to system size, metalization is more persistent than localization at the edges when the flakes get smaller.

Table 2 presents huge values of tensile strain. It should be noted that nanomaterials are capable of sustaining higher strains than their bulk counterparts; even in epitaxial growth, which poses a strong limit on the values of strain in 2D materials, it is possible to grow nanowires and nanodisks with small radii with high values of strain, from 3% to 7% and up to 10 % in some cases, stemming from their small lateral size. This lateral thickness is minimal in flakes of 2D materials, so the tolerance to mismatch will be even larger, see [44].

4. Conclusions

In summary, we have revealed the obstructed phase of the monolayer $PdSe_2$ and characterized it by topological invariants and the presence of corner charges. This 2D pentagonal material exhibits robustness against spatial perturbations due to the protection provided by inversion symmetry. About other materials similar to $PdSe_2$, such as the pentagonal allotropes of PdS_2, $PdTe_2$, $PtSe_2$, PtS_2, and $PtTe_2$, further investigations can be conducted to explore their electronic properties and potential topological phases. These materials may exhibit similar characteristics and symmetry-based topological band structures; see for example figure S2 in the supplementary information, which presents the spectrum of a $PtSe_2$ flake.

Metallic obstructed states could be spotted by atomic force microscopy (AFM), detecting the electrostatic forces produced by the corner charges. This could be achieved by employing conductivity AFM and scanning quantum dot microscopy, as suggested in [45]. A potential and promising experimental application recently proposed is related to catalysis: obstructed surface states show an enhanced catalytic response at the boundary of the structure, i.e. at the corner states, different from that at the inner regions of the flakes [46].

Extensions of this work could involve studying the implications of the valence band phase in optical responses. This would imply investigating the optical properties, such as absorption, emission, and polarization of the material in the presence of the non-trivial phase. The understanding of the interplay between the valence-band phase and the strong topology of the low-lying conduction bands, it is another avenue for exploration. This would provide insights into the electronic structure and potential applications in electronic and optoelectronic devices.

Overall, these extensions would contribute to a deeper understanding of the electronic and optical properties of materials with similar characteristics to $PdSe_2$, paving the way for advancements in topological materials and their technological applications.

4.1. Computational details

We have utilized the SIESTA [47] and QUANTUM ESPRESSO (QE) [48, 49] codes, employing the PBE generalized gradient approximation for exchange-correlation functional [33]. The vacuum spacing between adjacent layers was set to 20 Å to prevent interaction with neighboring periodic replicas. With the QE code, we relaxed the pentagonal structures with a cutoff energy of 80 Ry, and a force tolerance of 10^{-5} eV Å^{-1} per atom along with a $12 \times 12 \times 1$ Monkhorst–Pack grid for total energy convergence. For flake-related calculations, we employed the SIESTA code with a fixed mesh cutoff of 450 Ry, an electronic temperature of 10 meV, and a selfconsistent field convergence tolerance of 10^{-5} for the density matrix. We used the Python package IrRep [50] to compute the irreducible representations (irreps) for the HSPs of the material. This tool calculates the symmetry eigenvalues of first-principles electronic Bloch states in crystalline solids and identifies the corresponding irreducible representations under which they transform.

Data availability statement

All data that support the findings of this study are included within the article (and any supplementary files).

Acknowledgments

V N and M P acknowledge the financial support of Chilean FONDECYT by Grant 1211913. S B acknowledges DGIIE (UTFSM) through the Postdoctoral initiative. L C acknowledges financial support from the Spanish Ministry of Science and Innovation Grant PID2022-136285NB-C31 funded by MCIN/AEI/10.13039/501100011033/, and Grant (MAD2D-CM)–(UCM5), Recovery, Transformation and Resilience Plan, funded by the European Union—NextGenerationEU. We thank Olga Arroyo Gascón for her critical reading of the manuscript.

Conflicts of interest

There are no conflicts to declare.

ORCID iDs

Leonor Chico https://orcid.org/0000-0002-7131-1266
M Pacheco https://orcid.org/0000-0002-4293-5213

References

[1] Fu L 2011 *Phys. Rev. Lett.* **106** 106802
[2] Schindler F, Cook A M, Vergniory M G, Wang Z, Parkin S S P, Bernevig B A and Neupert T 2018 *Sci. Adv.* **4** eaat0346
[3] Benalcazar W A, Bernevig B A and Hughes T L 2017 *Phys. Rev.* B **96** 245115
[4] Xie B, Wang H-X, Zhang X, Zhan P, Jiang J-H, Lu M and Chen Y 2021 *Nat. Rev. Phys.* **3** 520–32
[5] Bradlyn B, Elcoro L, Cano J, Vergniory M G, Wang Z, Felser C, Aroyo M I and Bernevig B A 2017 *Nature* **547** 298–305
[6] Xu Y, Elcoro L, Song Z D, Vergniory M G, Felser C, Parkin S S P, Regnault N, Mañes J L and Bernevig B A 2021 Filling-enforced obstructed atomic insulators (arXiv:2106.10276)
[7] Lee E, Kim R, Ahn J and Yang B-J 2020 *npj Quantum Mater.* **5** 1
[8] Sheng X-L, Chen C, Liu H, Chen Z, Yu Z-M, Zhao Y X and Yang S A 2019 *Phys. Rev. Lett.* **123** 256402
[9] Liu B, Zhao G, Liu Z and Wang Z F 2019 *Nano Lett.* **19** 6492–7
[10] Hitomi M, Kawakami T and Koshino M 2021 *Phys. Rev.* B **104** 125302
[11] Pan M, Li D, Fan J and Huang H 2022 *npj Comput. Mater.* **8** 1
[12] Ezawa M 2019 *Sci. Rep.* **9** 5286
[13] Zeng J, Liu H, Jiang H, Sun Q-F and Xie X C 2021 *Phys. Rev.* B **104** L161108
[14] Qian S, Liu G-B, Liu C-C and Yao Y 2022 *Phys. Rev.* B **105** 045417
[15] Guo Z, Deng J, Xie Y and Wang Z 2022 *npj Quantum Mater.* **7** 87
[16] Wang L, Jiang Y, Liu J, Zhang S, Li J, Liu P, Sun Y, Weng H and Chen X-Q 2022 *Phys. Rev.* B **106** 155144
[17] Mao N, Li R, Dai Y, Huang B, Yan B and Niu C 2022 *Adv. Sci.* **9** 2202564
[18] Gao J, Qian Y, Jia H, Guo Z, Fang Z, Liu M, Weng H and Wang Z 2022 *Sci. Bull.* **67** 598–608
[19] Oyedele A D *et al* 2019 *J. Am. Chem. Soc.* **141** 8928–36
[20] Oyedele A D *et al* 2020 *Adv. Opt. Mater.* **8** 1901792
[21] Shen Y and Wang Q 2022 *Phys. Rep.* **964** 1–42
[22] Zhao Y, Yu P, Zhang G, Sun M, Chi D, Hippalgaonkar K, Thong J T L and Wu J 2020 *Adv. Funct. Mater.* **30** 2004896
[23] Bravo S, Pacheco M, Correa J D and Chico L 2022 *Phys. Chem. Chem. Phys.* **24** 15749
[24] Po H C, Vishwanath A and Watanabe H 2017 *Nat. Commun.* **8** 50
[25] Kruthoff J, de Boer J, van Wezel J, Kane C L and Slager R J 2017 *Phys. Rev.* X **7** 041069
[26] Aroyo M I, Perez-Mato J M, Capillas C, Kroumova E, Ivantchev S, Madariaga G, Kirov A and Wondratschek H 2006 *Z. Kristallogr.* **221** 15–27
[27] Savin A, Nesper R, Wengert S and Fässler T F 1997 *Angew. Chem., Int. Ed. Engl.* **36** 1808–32
[28] Xu X-W, Li Y-Z, Liu Z-F and Chen A-X 2020 *Phys. Rev.* A **101** 063839
[29] Liu F and Wakabayashi K 2017 *Phys. Rev. Lett.* **118** 076803
[30] Zhu L, Prodan E and Ahn K H 2019 *Phys. Rev.* B **99** 041117
[31] Obana D, Liu F and Wakabayashi K 2019 *Phys. Rev.* B **100** 075437
[32] Jeon S and Kim Y 2022 *Phys. Rev.* B **105** L121101
[33] Perdew J P, Burke K and Ernzerhof M 1996 *Phys. Rev. Lett.* **77** 3865–8
[34] Cano J and Bradlyn B 2021 *Annu. Rev. Condens. Matter Phys.* **12** 225–46
[35] Schindler F, Brzezińska M, Benalcazar W A, Iraola M, Bouhon A, Tsirkin S S, Vergniory M G and Neupert T 2019 *Phys. Rev. Res.* **1** 033074
[36] Benalcazar W A, Li T and Hughes T L 2019 *Phys. Rev.* B **99** 245151
[37] Vanderbilt D 2018 *Berry Phases in Electronic Structure Theory: Electric Polarization, Orbital Magnetization and Topological Insulators* (Cambridge University Press)
[38] Jiang S *et al* 2019 *Small* **15** 1902789
[39] Ren S, Souza I and Vanderbilt D 2021 *Phys. Rev.* B **103** 035147
[40] Trifunovic L 2020 *Phys. Rev. Res.* **2** 043012
[41] Elcoro L, Song Z and Bernevig B A 2020 *Phys. Rev.* B **102** 035110
[42] Khalaf E, Benalcazar W A, Hughes T L and Queiroz R 2021 *Phys. Rev. Res.* **3** 013239
[43] Liu F and Wakabayashi K 2021 *Phys. Rev. Res.* **3** 023121
[44] Ning C-Z, Dou L and Yang P 2017 *Nat. Rev. Mater.* **2** 17070
[45] Wagner C, Green M F B, Leinen P, Deilmann T, Krüger P, Rohlfing M, Temirov R and Tautz F S 2015 *Phys. Rev. Lett.* **115** 026101
[46] Li G *et al* 2022 *Adv. Mater.* **34** 2201328
[47] Soler J M, Artacho E, Gale J D, García A, Junquera J, Ordejón P and Sánchez-Portal D 2002 *J. Phys.: Condens. Matter* **14** 2745
[48] Giannozzi P *et al* 2009 *J. Phys.: Condens. Matter* **21** 395502
[49] Giannozzi P *et al* 2017 *J. Phys.: Condens. Matter* **29** 465901
[50] Iraola M, Mañes J L, Bradlyn B, Neupert T, Vergniory M G and Tsirkin S S 2022 *Comput. Phys. Commun.* **272** 108226